Certified Descent Algorithm for shape optimization driven by fully-computable a posteriori error estimators

Matteo Giacomini, Olivier Pantz, Karim Trabelsi

Certified Descent Algorithm for shape optimization driven by fully-computable a posteriori error estimators

M. Giacomini [*,†], O. Pantz [‡] and K. Trabelsi [†]

Abstract

In this paper we introduce a novel certified shape optimization strategy -named Certified Descent Algorithm (CDA) - to account for the numerical error introduced by the Finite Element approximation of the shape gradient. We present a goal-oriented procedure to derive a certified upper bound of the error in the shape gradient and we construct a fully-computable, constant-free *a posteriori* error estimator inspired by the complementary energy principle. The resulting CDA is able to identify a genuine descent direction at each iteration and features a reliable stopping criterion. After validating the error estimator, some numerical simulations of the resulting certified shape optimization strategy are presented for the well-known inverse identification problem of Electrical Impedance Tomography.

Keywords: Shape optimization; A posteriori error estimator; Certified Descent Algorithm; Electrical Impedance Tomography

1 Introduction

Shape optimization is a class of optimization problems in which the objective functional depends on the shape of the domain in which a Partial Differential Equation (PDE) is formulated and on the solution of the PDE itself. Thus, we may view these problems as PDE-constrained optimization problems of a shape-dependent functional, the domain being the optimization variable and the PDE being the constraint. This class of problems has been tackled in the literature using both gradient-based and gradient-free methods and in this work we consider a strategy issue of the former group by computing the so-called shape gradient.

In most applications, the differential form of the objective functional with respect to the shape depends on the solution of a PDE which usually can only be solved approximately by means of a discretization strategy like the Finite Element Method. The approximation of the governing equation

[*]CMAP Ecole Polytechnique, Route de Saclay, 91128 Palaiseau, France.
[†]DRI Institut Polytechnique des Sciences Avancées, 7-9 rue M. Grandcoing, 94200 Ivry-sur-Seine, France.
[‡]Laboratoire J.A. Dieudonné UMR 7351 CNRS-Université de Nice-Sophia Antipolis, Parc Valrose, 06108 Nice Cedex 02, France.

M. Giacomini and O. Pantz are members of the DEFI team at INRIA Saclay Île-de-France.
This work has been partially supported by the FMJH (Fondation Mathématique Jacques Hadamard) through a PGMO Gaspard Monge Project.

e-mail: matteo.giacomini@polytechnique.edu; olivier.pantz@polytechnique.org; trabelsi@ipsa.fr

for the phenomenon under analysis introduces an uncertainty which may prevent the shape gradient from being strictly negative along the identified descent direction, that is, the approximated direction may not lead to any improvement of the objective functional we are trying to optimize. Moreover, due to the aforementioned approximation, stopping criteria based on the norm of the shape gradient may never be fulfilled if the *a priori* given tolerance is too small with respect to the chosen discretization. Within this framework, *a posteriori* error estimators provide useful information to improve gradient-based algorithms for shape optimization.

Several works in the literature have highlighted the great potential of coupling *a posteriori* error estimators to shape optimization algorithms. In the pioneering work [6], the authors identify two different sources for the numerical error: on the one hand, the error arising from the approximation of the differential problem and on the other hand, the error due to the approximation of the geometry. Starting from this observation, Banichuk *et al.* present a first attempt to use the information on the discretization of the differential problem provided by a recovery-based estimator and the error arising from the approximation of the geometry to develop an adaptive shape optimization strategy. This work has been later extended by Morin *et al.* in [20], where the adaptive discretization of the governing equations by means of the Adaptive Finite Element Method is linked to an adaptive strategy for the approximation of the geometry. The authors derive estimators of the numerical error that are later used to drive an Adaptive Sequential Quadratic Programming algorithm to appropriately refine and coarsen the computational mesh. Several other authors have used adaptive techniques for the approximation of PDE's in order to improve the accuracy of the solution and obtain better final configurations in optimal structural design problems. We refer to [2, 17, 25, 27] for some examples. We remark that in all these works, *a posteriori* estimators only provide qualitative information about the numerical error due to the discretization of the problems and are essentially used to drive mesh adaptivity procedures. To the best of our knowledge, no guaranteed fully-computable estimate has been investigated and the error in the shape gradient itself is not accounted for, thus preventing reliable stopping criteria to be derived.

In the present paper, the derivation of a fully-computable upper bound for the error in the shape gradient is tackled. We neglect the contribution of the approximation of the geometry and we focus on the error arising from the discretization of the governing equation. The quantitative estimate of the error due to the numerical approximation of the shape gradient allows to identify a genuine descent direction and to introduce a reliable stopping criterion for the overall optimization strategy. We propose a novel shape optimization strategy - named Certified Descent Algorithm (CDA) - that generates a sequence of minimizing shapes by certifying at each iteration the descent direction to be genuine and automatically stops when a reliable stopping criterion is fulfilled.

The rest of the paper is organized as follows. First, we introduce the general framework of shape optimization and shape identification problems and the so-called Boundary Variation Algorithm (Section 2). In section 3, we account for the discretization error in the Quantity of Interest using the framework presented in [21]. Then, we introduce the resulting Certified Descent Algorithm that couples the *a posteriori* error estimator and the Boundary Variation Algorithm to derive a genuine descent direction for the shape optimization problem (Section 4). In section 5, we present the application of the Certified Descent Algorithm to the inverse problem of Electrical Impedance Tomography (EIT): after introducing the formulation of the identification problem as a shape optimization problem, we derive a fully-computable upper bound of the error in the shape gradient using the complementary energy principle. Eventually, in section 6 we present some numerical tests of the application of CDA

to the EIT problem and section 7 summarizes our results.

2 Shape optimization and shape identification problems

We consider an open domain $\Omega \subset \mathbb{R}^d$ ($d \geq 2$) with Lipschitz boundary $\partial\Omega$. Let V_Ω be a separable Hilbert space depending on Ω, we define $u_\Omega \in V_\Omega$ to be the solution of a state equation which is a linear PDE in the domain Ω:

$$a_\Omega(u_\Omega, \delta u) = F_\Omega(\delta u) \qquad \forall \delta u \in V_\Omega \tag{2.1}$$

where $a_\Omega(\cdot,\cdot) : V_\Omega \times V_\Omega \to \mathbb{R}$ is a continuous bilinear form satisfying the inf-sup condition

$$\inf_{w\in V_\Omega} \sup_{v\in V_\Omega} \frac{a_\Omega(v,w)}{\|v\|\|w\|} = \inf_{v\in V_\Omega} \sup_{w\in V_\Omega} \frac{a_\Omega(v,w)}{\|v\|\|w\|} > 0$$

and $F_\Omega(\cdot)$ is a continuous linear form on V_Ω, both of them depending on Ω. Under these assumptions, problem (2.1) has a unique solution u_Ω.

We introduce a cost functional $J(\Omega) = j(\Omega, u_\Omega)$ which depends on the domain Ω itself and on the solution u_Ω of the state equation. We consider the following shape optimization problem

$$\min_{\Omega\in\mathcal{U}_{\text{ad}}} J(\Omega) \tag{2.2}$$

where $\mathcal{U}_{\text{ad}}$ is the set of admissible domains in $\mathbb{R}^d$. Within this framework, problem (2.2) may be viewed as a PDE-constrained optimization problem, in which we aim at minimizing the functional $j(\Omega, u)$ under the constraint $u = u_\Omega$, that is the minimizer u is solution of the state equation (2.1).
In the following subsections, we recall the notion of shape gradient of $J(\Omega)$ in the direction θ and we apply the Steepest Descent Method to the shape optimization problem (2.2).

2.1 Differentiation with respect to the shape

Let $X \subset W^{1,\infty}(\Omega;\mathbb{R}^d)$ be a Banach space and $\theta \in X$ be an admissible smooth deformation of Ω. The cost functional $J(\Omega)$ is said to be X-differentiable at $\Omega \in \mathcal{U}_{\text{ad}}$ if there exists a continuous linear form $dJ(\Omega)$ on X such that $\forall \theta \in X$

$$J((\mathrm{Id}+\theta)\Omega) = J(\Omega) + \langle dJ(\Omega), \theta\rangle + o(\theta).$$

Several approaches are feasible to compute the shape gradient. Here we briefly recall the fast derivation method by Céa [9] and the material derivative approach [28]. Let us introduce the Lagrangian functional, defined for every admissible open set Ω and every $u,\ p \in V_\Omega$ by

$$\mathcal{L}(\Omega, u, p) = j(\Omega, u) + a_\Omega(u, p) - F_\Omega(p). \tag{2.3}$$

Let $p_\Omega \in V_\Omega$ be the solution of the so-called adjoint problem, that is

$$a^*_\Omega(p_\Omega, \delta p) + \left\langle \frac{\partial j}{\partial u}(\Omega, u_\Omega), \delta p \right\rangle = 0 \qquad \forall \delta p \in V_\Omega \tag{2.4}$$

where $a^*_\Omega(p, \delta p) = a_\Omega(\delta p, p)$ is the adjoint bilinear form. By applying the fast derivation method by Céa, we get the following expression of the shape gradient:

$$\langle dJ(\Omega), \theta \rangle = \left\langle \frac{\partial \mathcal{L}}{\partial \Omega}(\Omega, u_\Omega, p_\Omega), \theta \right\rangle. \tag{2.5}$$

An alternative procedure to compute the shape gradient relies on the definition of a diffeomorphism $\varphi : \mathbb{R}^d \to \mathbb{R}^d$ such that for every admissible set Ω

$$\Omega_\varphi \coloneqq \varphi(\Omega).$$

Moreover, all functions $u,\ p \in V_\Omega$ defined on the reference domain Ω may be mapped to the deformed domain Ω_φ by

$$u_\varphi \coloneqq u \circ \varphi^{-1} \qquad \text{and} \qquad p_\varphi \coloneqq p \circ \varphi^{-1}.$$

We admit that $u \mapsto u_\varphi$ is a one-to-one map between V_Ω and $V_{\varphi(\Omega)}$. The Lagrangian (2.3) is said to admit a material derivative if there exists a linear form $\frac{\partial \mathcal{L}}{\partial \varphi}$ such that

$$\mathcal{L}(\Omega_\varphi, u_\varphi, p_\varphi) = \mathcal{L}(\Omega, u, p) + \left\langle \frac{\partial \mathcal{L}}{\partial \varphi}(\Omega, u, p), \theta \right\rangle + o(\theta)$$

where $\varphi = \mathrm{Id} + \theta$. Provided that u_φ is differentiable with respect to φ at $\varphi = \mathrm{Id}$ in $V_{\varphi(\Omega)}$, from the fast derivation method of Céa we obtain the following expression for the shape gradient:

$$\langle dJ(\Omega), \theta \rangle = \left\langle \frac{\partial \mathcal{L}}{\partial \varphi}(\Omega, u_\Omega, p_\Omega), \theta \right\rangle. \tag{2.6}$$

A variant of the latter method consists in computing the shape gradient via the Lagrangian formulation without explicitly constructing the material derivative of the state and adjoint solutions. We refer to [19] for additional information about this approach.

Volumetric and surface expressions of the shape gradient

The most common approach in the literature to compute the shape gradient is based on an Eulerian point of view and leads to a surface expression of the shape gradient.
The main advantage of this method relies on the fact that the boundary representation intuitively provides an explicit expression for the descent direction. Let us assume that the shape gradient has the following form

$$\langle dJ(\Omega), \theta \rangle = \int_{\partial\Omega} h\theta \cdot n ds$$

then $\theta = -hn$ on $\partial\Omega$ is a descent direction. Moreover, by Hadamard-Zolésio structure theorem it is well-known that the shape gradient is carried on the boundary of the shape [11] and using this approach the descent direction has to be defined only on $\partial\Omega$. Nevertheless, if the boundary datum of the state problem is not sufficiently smooth, the surface expression of the shape gradient may not exist or the descent direction θ may suffer from poor regularity.
Starting from the surface representation of the shape gradient, it is possible to derive a volumetric expression as well. Though the two expressions are equivalent in a continuous framework, they usually

are not when considering their numerical counterparts, i.e. their Finite Element approximations: as a matter of fact, in [16] Hiptmair *et al.* prove that the volumetric formulation generally provides better accuracy when using the Finite Element Method. Moreover, we may be able to derive the volumetric expression of the shape gradient even when its boundary representation fails to exist.
In this work, we consider the volumetric expression of the shape gradient in order to take advantage of the better accuracy it provides from a numerical point of view and to construct an estimator of the error in a Quantity of Interest using the procedure described by Oden and Prudhomme in [21].
We remark that in order to derive a descent direction θ on Ω from the volumetric expression of the shape gradient, an additional variational problem has to be solved, as described in next subsection.

2.2 The Boundary Variation Algorithm

From now on, we consider X to be a Hilbert space. Starting from the formulation (2.6), we seek a descent direction for the functional $J(\Omega)$. For this purpose, we solve an additional variational problem and we seek $\theta \in X$ such that

$$(\theta, \delta\theta)_X + \langle dJ(\Omega), \delta\theta \rangle = 0 \qquad \forall \delta\theta \in X. \tag{2.7}$$

Remark 2.1. The choice of the scalar product in (2.7) is a key point for the development of an efficient shape optimization method. In [5], the authors propose the so-called traction method to get rid of some irregularity issues in shape optimization problems. This approach is based on the regularization of the descent direction by means of a scalar product inspired by the linear elasticity equation. In recent years, a comparison of the L^2, H^1 and H^{-1} scalar products defined on a surface was presented [12] but, as the authors state, the best choice is strongly dependent on the application of interest.

In this section, we present the application of the Steepest Descent Method to a shape optimization problem. After computing the solution of the state equation, we solve the adjoint problem to derive the expression of the shape gradient. Then, a descent direction is identified through (2.7) and is used to deform the domain. The resulting shape optimization strategy is known in the literature as Boundary Variation Algorithm [3] and is sketched in script 1.

Algorithm 1: Continuous gradient method - The Boundary Variation Algorithm

Given the domain Ω_0, set $\ell = 0$ and iterate:
1. Compute the solution u_{Ω_ℓ} of the state equation;
2. Compute the solution p_{Ω_ℓ} of the adjoint equation;
3. Compute a descent direction $\theta_\ell \in X$ solving $(\theta_\ell, \delta\theta)_X + \langle dJ(\Omega_\ell), \delta\theta \rangle = 0 \quad \forall \delta\theta \in X$;
4. Identify an admissible step μ_ℓ;
5. Update the domain $\Omega_{\ell+1} = (\mathrm{Id} + \mu_\ell \theta_\ell)\Omega_\ell$;
6. While $|\langle dJ(\Omega_\ell), \theta_\ell \rangle| >$ tol, $\ell = \ell + 1$ and repeat.

We remark that this method relies on the computation at each iteration of a direction θ such that the shape gradient of the objective functional in this direction is strictly negative, that is we seek θ such that $\langle dJ(\Omega), \theta \rangle < 0$. In next subsection, we discuss the modifications that occur when moving from the continuous to the discretized formulation of the problems and consequently the conditions that the discretization of θ has to fulfill in order to be a genuine descent direction for the functional $J(\Omega)$.

2.3 The discretized Boundary Variation Algorithm

Let us denote by u_Ω^h and p_Ω^h the approximations of the state and adjoint equations arising from a Finite Element discretization. The discretized direction $\theta^h \in X$ is obtained by solving problem (2.8)

$$(\theta^h, \delta\theta)_X + \langle d_h J(\Omega), \delta\theta \rangle = 0 \qquad \forall \delta\theta \in X \tag{2.8}$$

where $\langle d_h J(\Omega), \delta\theta \rangle$ reads as follows:

$$\langle d_h J(\Omega), \delta\theta \rangle \coloneqq \left\langle \frac{\partial \mathcal{L}}{\partial \varphi}(\Omega, u_\Omega^h, p_\Omega^h), \delta\theta \right\rangle. \tag{2.9}$$

The discretized version of the Boundary Variation Algorithm is derived by substituting the continuous functions u_Ω, p_Ω with their approximations u_Ω^h, p_Ω^h and θ with θ^h:

Algorithm 2: Discretized gradient method - The discretized Boundary Variation Algorithm

Given the domain Ω_0, set $\ell = 0$ and iterate:
1. Compute the solution $u_{\Omega_\ell}^h$ of the state equation;
2. Compute the solution $p_{\Omega_\ell}^h$ of the adjoint equation;
3. Compute a descent direction $\theta_\ell^h \in X$ solving $(\theta_\ell^h, \delta\theta)_X + \langle d_h J(\Omega_\ell), \delta\theta \rangle = 0 \quad \forall \delta\theta \in X$;
4. Identify an admissible step μ_ℓ;
5. Update the domain $\Omega_{\ell+1} = (\mathrm{Id} + \mu_\ell \theta_\ell^h)\Omega_\ell$;
6. While $|\langle d_h J(\Omega_\ell), \theta_\ell^h \rangle| >$ tol, $\ell = \ell + 1$ and repeat.

We remark that due to the numerical error introduced by the Finite Element discretization, even though $\langle d_h J(\Omega), \theta^h \rangle < 0$, θ^h is not necessarily a genuine descent direction for the functional $J(\Omega)$. Moreover, it is important to notice that the stopping criterion (Algorithm 2 - step 6) will usually not be fulfilled if the required tolerance `tol` is too sharp with respect to the chosen discretization.
In the following sections, we present a strategy to bypass these issues by providing a computable upper bound of the error E^h in the approximation of the shape gradient (Section 3). Then, in section 4 we couple the information embedded in the estimator with the Boundary Variation Algorithm (Script 1) by introducing the novel Certified Descent Algorithm in which at each iteration we seek a certified descent direction, that is θ^h that satisfies $\langle d_h J(\Omega), \theta^h \rangle + |E^h| < 0$.

3 Numerical error in the shape gradient

Let us consider the error E^h in the shape gradient:

$$E^h = \langle dJ(\Omega) - d_h J(\Omega), \theta^h \rangle. \tag{3.1}$$

The strategy presented in this section to estimate the *a posteriori* error in a Quantity of Interest - namely, the shape gradient - is derived from the work [21] by Oden and Prudhomme. Basic idea relies on the definition of an adjoint problem whose right-hand side is the quantity whose error estimate is sought.

3.1 Variational formulation of the error in the QoI

Let us rewrite the numerical error E^h in the shape gradient as follows

$$\begin{aligned} E^h &= \left\langle \frac{\partial \mathcal{L}}{\partial \varphi}(\Omega, u_\Omega, p_\Omega) - \frac{\partial \mathcal{L}}{\partial \varphi}(\Omega, u_\Omega^h, p_\Omega^h), \theta^h \right\rangle \\ &\simeq \frac{\partial^2 \mathcal{L}}{\partial \varphi \partial u}(\Omega, u_\Omega^h, p_\Omega^h)[\theta^h, u_\Omega - u_\Omega^h] + \frac{\partial^2 \mathcal{L}}{\partial \varphi \partial p}(\Omega, u_\Omega^h, p_\Omega^h)[\theta^h, p_\Omega - p_\Omega^h] =: \widetilde{E}^h. \end{aligned} \tag{3.2}$$

The computation of an upper bound of the error (3.2) is performed using the well-established framework of *a posteriori* error estimators in a Quantity of Interest [21]. For this purpose we introduce two adjoint problems, each of which is associated with one term on the right-hand side of (3.2). Thus, we seek $r_\Omega, s_\Omega \in V_\Omega$ such that

$$\begin{aligned} a_\Omega^*(r_\Omega, \delta r) &= \frac{\partial^2 \mathcal{L}}{\partial \varphi \partial u}(\Omega, u_\Omega^h, p_\Omega^h)[\theta^h, \delta r] \qquad \forall \delta r \in V_\Omega \\ a_\Omega^*(s_\Omega, \delta s) &= \frac{\partial^2 \mathcal{L}}{\partial \varphi \partial p}(\Omega, u_\Omega^h, p_\Omega^h)[\theta^h, \delta s] \qquad \forall \delta s \in V_\Omega \end{aligned} \tag{3.3}$$

where, as previously stated, $a_\Omega^*(\cdot,\cdot)$ is the adjoint bilinear form. We remark that in order for the aforementioned adjoint problems to be well-posed, their right-hand sides have to be linear and continuous forms on V_Ω. Several works as [13] and [26] have dealt with an extension of the original framework in [21] to the case of non-linear Quantities of Interest. We follow the approach proposed by these authors by performing a linearization of the functional whose error estimate is sought and we introduce the linearized error $\widetilde{E}^h$ in (3.2).

We denote by r_Ω^h, s_Ω^h the approximations of the solutions r_Ω, s_Ω of equations (3.3) arising from a Finite Element discretization. By plugging (3.3) into (3.2), we may derive the following upper bound $\overline{E}$ for the numerical error in the shape gradient:

$$\begin{aligned} |E^h| \simeq |\widetilde{E}^h| &\leq |a_\Omega^*(r_\Omega - r_\Omega^h, u_\Omega - u_\Omega^h)| + |a_\Omega^*(s_\Omega - s_\Omega^h, p_\Omega - p_\Omega^h)| \\ &\leq \; |\!|\!| r_\Omega - r_\Omega^h |\!|\!|_\Omega \, |\!|\!| u_\Omega - u_\Omega^h |\!|\!|_\Omega + \; |\!|\!| s_\Omega - s_\Omega^h |\!|\!|_\Omega \, |\!|\!| p_\Omega - p_\Omega^h |\!|\!|_\Omega =: \overline{E} \end{aligned} \tag{3.4}$$

where $|\!|\!| \cdot |\!|\!|_\Omega$ is the energy-norm induced by the bilinear form $a_\Omega(\cdot,\cdot)$. The first inequality follows from triangle inequality and Galerkin orthogonality whereas the upper bound $\overline{E}$ is derived exploiting Cauchy-Schwarz inequality.

Remark 3.1. In (3.4) we derived an upper bound for the numerical error in the linearized shape gradient and not in the shape gradient itself. For the rest of this paper, we will follow the framework in [13] by assuming the linearization error to be negligible and $\overline{E}$ to be an upper bound of the numerical error E^h itself and not of its linearized version $\widetilde{E}^h$. In section 6.1, a validation of the error estimator is presented for the case of Electrical Impedance Tomography: we will verify that the linearization error is indeed negligible with respect to the error due to the Finite Element discretization and thus the previous assumption stands.

In order to fully compute the error estimator (3.4), we have to estimate the energy-norm of the error for:

- the state equation;

- the adjoint equation used to compute the shape gradient;
- the two adjoint equations associated with the Quantity of Interest.

Several strategies are possible to tackle these issues. In this paper, we propose a method inspired by the complementary energy principle which allows to derive fully-computable, constant-free estimators by solving an additional variational problem for each term under analysis in order to retrieve a flux estimate. These estimates are problem-dependent and will be detailed in section 5 when presenting the case of Electrical Impedance Tomography.

3.2 Computing a certified descent direction

In the previous section, we derived a guaranteed upper bound of the error (3.1) due to the numerical approximation of the shape gradient. As previously stated, $\langle d_h J(\Omega), \theta^h \rangle < 0$ does not imply that the direction θ^h is a genuine descent direction. Nevertheless, we may bypass this issue using the information carried by the upper bound $\overline{E}$ of the error E^h, thus seeking a direction θ^h such that

$$\langle d_h J(\Omega), \theta^h \rangle + \overline{E} < 0. \tag{3.5}$$

The direction θ^h fulfilling condition (3.5) is said to be certified because owing to the *a posteriori* error estimator it is guaranteed that the original functional $J(\Omega)$ decreases along θ^h whenever the linearization error introduced in (3.2) is negligible. We remark that the criterion (3.5) ensures that θ^h is a genuine descent direction, whether it is the solution of equation (2.8) or not. In particular, this also stands when the latter problem is only solved approximately.
Hence, on the one hand the computation of the upper bound of the numerical error in the shape gradient provides useful information to identify a certified descent direction at each iteration of the optimization algorithm and to construct a certified shape optimization strategy. On the other hand, the fully-computable and constant-free error estimator allows to establish a quantitative criterion to derive a reliable stopping criterion for the overall optimization procedure.

4 The Certified Descent Algorithm

We are now ready to introduce the novel Certified Descent Algorithm, arising from the coupling of the Boundary Variation Algorithm for shape optimization (Section 2.2) and the goal-oriented estimator for the error in the shape gradient (Section 3.1).
In script 3, we present a variant of algorithm 1 that takes advantage of the previously introduced *a posteriori* estimator for the error in the shape gradient in order to bypass the issues due to the discretization of the problem.

First, the procedure constructs an initial computational domain. At each iteration, the algorithm solves the state and adjoint problems [steps 1 and 2] and computes a descent direction θ^h solving equation (2.8) [step 3]. Then, the adjoint problems (3.3) are solved and an upper bound of the numerical error in the shape gradient along the direction θ^h is computed [step 4]. If condition (3.5) is not fulfilled, the mesh is adapted in order to improve the error estimate. This procedure is iterated until the direction θ^h is a certified descent direction for $J(\Omega)$ [step 5]. Once a certified descent direction has been identified, we compute a step [step 6] such that the following Armijo condition is fulfilled:

let us consider the iteration ℓ, given $0 < \alpha < 1$ we use a backtracking strategy to identify the step $\mu_\ell \in \mathbb{R}^+$ such that

$$J\left(\left(\mathrm{Id} + \mu_\ell \theta_\ell^h\right)\Omega_\ell\right) \leq J\left(\Omega_\ell\right) + \alpha\mu_\ell \langle d_h J\left(\Omega_\ell\right), \theta_\ell^h \rangle.$$

An alternative bisection-based line search technique has been proposed by Morin *et al.* in [20].
Then the shape of the domain is updated according to the computed perturbation of the identity $\mathrm{Id} + \mu_\ell \theta_\ell^h$ [step 7]. Eventually, a novel stopping criterion is proposed [step 8] in order to use the information embedded in the error bound $\overline{E}$ to derive a reliable condition to end the evolution of the algorithm.

Algorithm 3: Discretized gradient method - The Certified Descent Algorithm

Given the domain Ω_0, set $\ell = 0$ and iterate:
1. Compute the solution $u^h_{\Omega_\ell}$ of the state equation;
2. Compute the solution $p^h_{\Omega_\ell}$ of the adjoint equation;
3. Compute a descent direction $\theta_\ell^h \in X$ solving $(\theta_\ell^h, \delta\theta)_X + \langle d_h J(\Omega_\ell), \delta\theta \rangle = 0 \quad \forall \delta\theta \in X$;
4. Compute an upper bound $\overline{E}$ of the numerical error $|E^h|$:
   (a) Compute the solutions $r^h_{\Omega_\ell}$ and $s^h_{\Omega_\ell}$ to estimate the error in the QoI;
   (b) Compute $\overline{E} = \|\!| r_{\Omega_\ell} - r^h_{\Omega_\ell} |\!\|_\Omega \, |\!\| u_{\Omega_\ell} - u^h_{\Omega_\ell} |\!\|_\Omega + |\!\| s_{\Omega_\ell} - s^h_{\Omega_\ell} |\!\|_\Omega \, |\!\| p_{\Omega_\ell} - p^h_{\Omega_\ell} |\!\|_\Omega$;
5. If $\langle d_h J(\Omega_\ell), \theta_\ell^h \rangle + \overline{E} \geq 0$, refine the mesh and go to 1;
6. Identify an admissible step μ_ℓ;
7. Update the shape $\Omega_{\ell+1} = (\mathrm{Id} + \mu_\ell \theta_\ell^h)\Omega_\ell$;
8. While $|\langle d_h J(\Omega_\ell), \theta_\ell^h \rangle| + \overline{E} >$ tol, $\ell = \ell + 1$ and repeat.

5 An inverse identification problem: the case of Electrical Impedance Tomography

Let us consider an open domain $\mathcal{D} \subset \mathbb{R}^2$. We suppose that there exists an open subdomain $\Omega \subset\subset \mathcal{D}$ such that some given physical properties of the problem under analysis are discontinuous along the interface $\partial\Omega$ between the inclusion Ω and the complementary set $\mathcal{D} \setminus \Omega$. The location and the shape of the inclusion are to be determined, thus Ω acts as unknown parameter in the state equations and in the inversion procedure. Our aim is to identify the inclusion Ω by performing non-invasive measurements on the boundary $\partial\mathcal{D}$ of the domain $\mathcal{D}$. This problem is well-known in the literature and is often referred to as Calderón's problem. Several review papers on Electrical Impedance Tomography have been published in the literature over the years. We refer to [7, 8, 10] for more details on the physical problem, its mathematical formulation and its numerical approximation.

Let χ_Ω be the characteristic function of the open set Ω, we define the conductivity k_Ω as a piecewise constant function such that $k_\Omega := k_I \chi_\Omega + k_E(1 - \chi_\Omega),\ k_I,\ k_E > 0$. We introduce two Boundary Value

Problems on the domain $\mathcal{D}$, respectively with Neumann and Dirichlet boundary conditions on $\partial\mathcal{D}$:

$$\begin{cases} -k_\Omega \Delta u_{\Omega,N} + u_{\Omega,N} = 0 & \text{in } \mathcal{D} \setminus \partial\Omega \\ [\![u_{\Omega,N}]\!] = 0 & \text{on } \partial\Omega \\ [\![k_\Omega \nabla u_{\Omega,N} \cdot n]\!] = 0 & \text{on } \partial\Omega \\ k_E \nabla u_{\Omega,N} \cdot n = g & \text{on } \partial\mathcal{D} \end{cases} \tag{5.1}$$

$$\begin{cases} -k_\Omega \Delta u_{\Omega,D} + u_{\Omega,D} = 0 & \text{in } \mathcal{D} \setminus \partial\Omega \\ [\![u_{\Omega,D}]\!] = 0 & \text{on } \partial\Omega \\ [\![k_\Omega \nabla u_{\Omega,D} \cdot n]\!] = 0 & \text{on } \partial\Omega \\ u_{\Omega,D} = U_D & \text{on } \partial\mathcal{D} \end{cases} \tag{5.2}$$

where the boundary data $g \in L^2(\partial\mathcal{D})$ and $U_D \in H^{\frac{1}{2}}(\partial\mathcal{D})$ arise from the performed physical measurements. As previously stated, we are interested in identifying the shape and the location of the inclusion, fitting given boundary measurements g and U_D of the flux and the potential.

5.1 State problems

In order to approximate problems (5.1) and (5.2) by means of the Finite Element Method, first we introduce their variational formulations.
Let $a_\Omega(\cdot,\cdot)$ be the bilinear form associated with both the problems and $F_{\Omega,i}(\cdot),\ i = N, D$ the linear forms respectively for the Neumann and the Dirichlet problem:

$$a_\Omega(u, \delta u) = \int_{\mathcal{D}} \Big(k_\Omega \nabla u \cdot \nabla \delta u + u \delta u \Big) dx \tag{5.3}$$

$$F_{\Omega,N}(\delta u) = \int_{\partial\mathcal{D}} g \delta u \ ds \qquad \text{and} \qquad F_{\Omega,D}(\delta u) = 0. \tag{5.4}$$

We consider $u_{\Omega,N},\ u_{\Omega,D} \in H^1(\mathcal{D})$ such that $u_{\Omega,D} = U_D$ on $\partial\mathcal{D}$, solutions of the following Neumann and Dirichlet variational problems $\forall \delta u_N \in H^1(\mathcal{D})$ and $\forall \delta u_D \in H^1_0(\mathcal{D})$:

$$a_\Omega(u_{\Omega,i}, \delta u_i) = F_{\Omega,i}(\delta u_i) \quad , \quad i = N, D. \tag{5.5}$$

For the Dirichlet problem, the non-homogeneous boundary datum is taken care of by means of a classical substitution technique. The corresponding discretized formulations of (5.5) may be derived by replacing the analytical solutions $u_{\Omega,N}$ and $u_{\Omega,D}$ with their approximations $u^h_{\Omega,N}$ and $u^h_{\Omega,D}$ which belong to the space of Lagrangian Finite Element functions. In a similar fashion, θ^h is the solution of equation (2.8) computed using a Lagrangian Finite Element space. The degree chosen for the Finite Element basis functions will be discussed in section 6.

5.2 A shape optimization approach

Let us consider the Kohn-Vogelius functional first introduced in [31] and later investigated by Kohn and Vogelius in [18]:

$$J(\Omega) = \frac{1}{2} \int_{\mathcal{D}} \Big(k_\Omega \left|\nabla(u_{\Omega,N} - u_{\Omega,D})\right|^2 + \left|u_{\Omega,N} - u_{\Omega,D}\right|^2 \Big) dx. \tag{5.6}$$

In (5.6), $u_{\Omega,N}$ and $u_{\Omega,D}$ respectively stand for the solutions of the state problems (5.1) and (5.2). Owing to (5.3), we may rewrite the objective functional (5.6) as:

$$J(\Omega) = \frac{1}{2} a_\Omega\Big(u_{\Omega,N} - u_{\Omega,D}, u_{\Omega,N} - u_{\Omega,D}\Big).$$

The inverse identification problem of Electrical Impedance Tomography may be written as the PDE-constrained optimization problem (2.2) in which we seek the open subset Ω that minimizes (5.6).
In order to solve this problem, we consider the Certified Descent Algorithm using the shape gradient of $J(\Omega)$. First, we need to determine the adjoint solutions $p_{\Omega,N}$ and $p_{\Omega,D}$ associated with the states $u_{\Omega,N}$ and $u_{\Omega,D}$: the Kohn-Vogelius problem is self-adjoint and we get that $p_{\Omega,N} = u_{\Omega,N} - u_{\Omega,D}$ and $p_{\Omega,D} = 0$. Let $\theta \in W^{1,\infty}(\mathcal{D};\mathbb{R}^2)$ be an admissible deformation of the domain such that $\theta = 0$ on $\partial\mathcal{D}$. As previously mentioned, the most common approach in the literature to compute the shape gradient leads to the surface expression

$$\langle dJ(\Omega), \theta\rangle = \frac{1}{2}\int_{\partial\Omega} \Big([\![k_\Omega]\!]\Big(\Big|\frac{\partial u_{\Omega,N}}{\partial\tau}\Big|^2 - \Big|\frac{\partial u_{\Omega,D}}{\partial\tau}\Big|^2\Big) - [\![k_\Omega^{-1}]\!]\Big(\Big|k_\Omega\frac{\partial u_{\Omega,N}}{\partial n}\Big|^2 - \Big|k_\Omega\frac{\partial u_{\Omega,D}}{\partial n}\Big|^2\Big)\Big)(\theta\cdot n)ds \tag{5.7}$$

where n is the outward normal to $\partial\Omega$, τ is the tangential direction to $\partial\Omega$ and $[\![k_\Omega]\!] = k_E - k_I$ and $[\![k_\Omega^{-1}]\!] = k_E^{-1} - k_I^{-1}$ are the jumps across $\partial\Omega$. Let us now introduce the following operator:

$$\langle G(\Omega,u),\theta\rangle = \frac{1}{2}\int_{\mathcal{D}} \Big(k_\Omega M(\theta)\nabla u\cdot\nabla u - \nabla\cdot\theta\ u^2\Big)dx \tag{5.8}$$

where $M(\theta) = \nabla\theta + \nabla\theta^T - (\nabla\cdot\theta)\,\mathrm{Id}$. From (2.6), we get the volumetric expression of the shape gradient of (5.6):

$$\langle dJ(\Omega),\theta\rangle = \langle G(\Omega,u_{\Omega,N}) - G(\Omega,u_{\Omega,D}),\theta\rangle. \tag{5.9}$$

We refer to [22] for more details on the differentiation of the Kohn-Vogelius functional and its application to the identification of discontinuities of the conductivity parameter.

5.3 *A posteriori* error estimate for the shape gradient

Since the Kohn-Vogelius problem is self-adjoint, (3.4) reduces to

$$\overline{E} = |\!|\!| r_{\Omega,N} - r^h_{\Omega,N} |\!|\!|_\Omega\, |\!|\!| u_{\Omega,N} - u^h_{\Omega,N} |\!|\!|_\Omega + |\!|\!| r_{\Omega,D} - r^h_{\Omega,D} |\!|\!|_\Omega\, |\!|\!| u_{\Omega,D} - u^h_{\Omega,D} |\!|\!|_\Omega \tag{5.10}$$

where $r_{\Omega,N}$ and $r_{\Omega,D}$ are the solutions of the adjoint problems introduced to evaluate the contributions of the Neumann and Dirichlet state problems to the error in the Quantity of Interest. Thus, we seek $r_{\Omega,N} \in H^1(\mathcal{D})$ and $r_{\Omega,D} \in H^1_0(\mathcal{D})$ such that respectively $\forall \delta r_N \in H^1(\mathcal{D})$ and $\forall \delta r_D \in H^1_0(\mathcal{D})$

$$a^*_\Omega(r_{\Omega,i},\delta r_i) = H_{\Omega,i}(\delta r_i) \quad , \quad i = N, D \tag{5.11}$$

where the linear forms on the right-hand sides of equations (5.11) read as

$$H_{\Omega,i}(\delta r) = \frac{\partial G}{\partial u}(\Omega, u^h_{\Omega,i})[\theta^h, \delta r] \quad , \quad i = N, D. \tag{5.12}$$

In order to obtain a computable upper bound for the error in the shape gradient, we seek an estimate of the energy-norm of the error for the state and adjoint solutions in (5.10).

Let $e_{\Omega,i} = u_{\Omega,i} - u^h_{\Omega,i}$ and $\epsilon_{\Omega,i} = r_{\Omega,i} - r^h_{\Omega,i}$ for $i = N, D$. In the following subsections, we derive the estimates of the energy-norm of the $e_{\Omega,i}$'s and the $\epsilon_{\Omega,i}$'s using a strategy inspired by the so-called complementary energy principle [24]. In practice, we introduce a dual flux variable for every problem and each bound is computed by solving an additional adjoint problem thus leading to a better approximation of the numerical fluxes $\nabla e_{\Omega,i}$'s and $\nabla \epsilon_{\Omega,i}$'s. For additional information on this approach, we refer to [30].

5.3.1 Error estimates based on the complementary energy principle: the case of the state equations

For the sake of readability, let us rename $H^1(\mathcal{D})$ as V_N and $H^1_0(\mathcal{D})$ as V_D. We consider the residual equations such that $\forall \delta u_N \in V_N$ and $\forall \delta u_D \in V_D$

$$a_\Omega(e_{\Omega,i}, \delta u_i) = F_{\Omega,i}(\delta u_i) - a_\Omega(u^h_{\Omega,i}, \delta u_i) \quad , \quad i = N, D. \tag{5.13}$$

We recall that solving equation (5.13) is equivalent to the following minimization problem, that is we seek $w \in V_i$ such that

$$E_{\Omega,i}(e_{\Omega,i}) = \min_{w \in V_i} E_{\Omega,i}(w) \quad , \quad i = N, D \tag{5.14}$$

where the global energy functional associated with the Neumann and Dirichlet problems reads

$$E_{\Omega,i}(w) = \frac{1}{2}\int_{\mathcal{D}} \Big(k_\Omega |\nabla w|^2 + |w|^2\Big) dx + \int_{\mathcal{D}} \Big(k_\Omega \nabla u^h_{\Omega,i} \cdot \nabla w + u^h_{\Omega,i} w\Big) dx - F_{\Omega,i}(w). \tag{5.15}$$

By introducing an additional variable $z = \nabla w$ and a dual variable $\sigma_{\Omega,i} \in L^2(\mathcal{D}; \mathbb{R}^d)$, we may construct the Lagrangian functional $L_{\Omega,i} : V_i \times L^2(\mathcal{D}) \times L^2(\mathcal{D}; \mathbb{R}^d) \to \mathbb{R}$ which has the following form

$$\begin{aligned} L_{\Omega,i}(w, z, \sigma_{\Omega,i}) =& \frac{1}{2}\int_{\mathcal{D}} \Big(k_\Omega |z|^2 + |w|^2\Big) dx + \int_{\mathcal{D}} \Big(k_\Omega \nabla u^h_{\Omega,i} \cdot z + u^h_{\Omega,i} w\Big) dx - F_{\Omega,i}(w) \\ &+ \int_{\mathcal{D}} \sigma_{\Omega,i} \cdot (\nabla w - z) dx. \end{aligned} \tag{5.16}$$

Thus the minimization problem (5.14) may be rewritten as a min-max problem and owing to the Lagrange duality, we get

$$\begin{aligned} \min_{w \in V_i} E_{\Omega,i}(w) &= \min_{\substack{w \in V_i \\ z = \nabla w}} \max_{\sigma_{\Omega,i} \in L^2(\mathcal{D}; \mathbb{R}^d)} L_{\Omega,i}(w, z, \sigma_{\Omega,i}) \\ &= \max_{\sigma_{\Omega,i} \in L^2(\mathcal{D}; \mathbb{R}^d)} \min_{\substack{w \in V_i \\ z = \nabla w}} L_{\Omega,i}(w, z, \sigma_{\Omega,i}). \end{aligned} \tag{5.17}$$

We consider the space $H(\mathrm{div}) = \{\sigma \in L^2(\mathcal{D}; \mathbb{R}^d) \ : \ \nabla \cdot \sigma \in L^2(\mathcal{D})\}$. Let $\sigma_{\Omega,i} \in H(\mathrm{div})$ for $i = N, D$, from the system of first-order optimality conditions for $L_{\Omega,i}(w, z, \sigma_{\Omega,i})$ we derive the following relationships among the variables:

$$\begin{cases} z = k_\Omega^{-1} \sigma_{\Omega,i} - \nabla u^h_{\Omega,i} & \text{in } \mathcal{D} \\ w = \nabla \cdot \sigma_{\Omega,i} - u^h_{\Omega,i} & \text{in } \mathcal{D} \\ \sigma_{\Omega,N} \cdot n = g & \text{on } \partial\mathcal{D} \end{cases} \tag{5.18}$$

Hence, by plugging (5.18) into (5.17), we get the following maximization problems for $i = N, D$

$$E_{\Omega,i}(e_{\Omega,i}) = \max_{\substack{\sigma_{\Omega,i}\in H(\mathrm{div}) \\ (\sigma_{\Omega,N}\cdot n = g)}} -\frac{1}{2}\int_{\mathcal{D}} \Big(k_\Omega^{-1}|\sigma_{\Omega,i} - k_\Omega \nabla u^h_{\Omega,i}|^2 + |\nabla\cdot\sigma_{\Omega,i} - u^h_{\Omega,i}|^2\Big)dx \tag{5.19}$$

where the objective functional is known as the dual complementary energy associated with the problems.

In order to compute the dual flux variables, we derive the first-order optimality conditions for the dual complementary energy functional in (5.19). Thus, we seek $\sigma_{\Omega,N},\ \sigma_{\Omega,D} \in H(\mathrm{div})$ such that $\sigma_{\Omega,N}\cdot n = g$ on $\partial\mathcal{D}$ which satisfy $\forall \delta\sigma_N,\ \delta\sigma_D \in H(\mathrm{div})$ such that $\delta\sigma_N \cdot n = 0$ on $\partial\mathcal{D}$

$$\int_{\mathcal{D}} \Big(k_\Omega^{-1}\sigma_{\Omega,i}\cdot\delta\sigma_i + (\nabla\cdot\sigma_{\Omega,i})(\nabla\cdot\delta\sigma_i)\Big)dx = \begin{cases} 0 & ,\ i = N \\ \int_{\partial\mathcal{D}} U_D(\delta\sigma_i\cdot n)ds & ,\ i = D \end{cases} \tag{5.20}$$

Let $\sigma^h_{\Omega,N}$ and $\sigma^h_{\Omega,D}$ be the dual fluxes discretized using Raviart-Thomas Finite Element functions. By combining the definition of energy-norm induced by the bilinear form (5.3) with the information in (5.18) and (5.20), we get the following upper bound for the energy-norm of the error in the state equations:

$$|\!|\!| u_{\Omega,i} - u^h_{\Omega,i} |\!|\!|^2_\Omega \le \int_{\mathcal{D}} \Big(k_\Omega^{-1}|\sigma^h_{\Omega,i} - k_\Omega\nabla u^h_{\Omega,i}|^2 + |\nabla\cdot\sigma^h_{\Omega,i} - u^h_{\Omega,i}|^2\Big)dx. \tag{5.21}$$

5.3.2 Error estimates based on the complementary energy principle: the case of the adjoint equations

As in the previous section, we present the formulation of the dual complementary energy associated with the discretization error of the adjoint problems (5.11). In a similar fashion, we introduce the dual fluxes $\xi_{\Omega,i} \in H(\mathrm{div})$ for $i = N, D$ and we retrieve the following relationships

$$\begin{cases} z = k_\Omega^{-1}\xi_{\Omega,i} + M(\theta^h)\nabla u^h_{\Omega,i} - \nabla r^h_{\Omega,i} & \text{in } \mathcal{D} \\ w = \nabla\cdot\xi_{\Omega,i} - \Big(\nabla\cdot\theta^h\Big)u^h_{\Omega,i} - r^h_{\Omega,i} & \text{in } \mathcal{D} \\ \xi_{\Omega,N}\cdot n = 0 & \text{on } \partial\mathcal{D} \end{cases} \tag{5.22}$$

The maximization problem for the dual complementary energy associated with the adjoint problems for $i = N, D$ reads as

$$\max_{\substack{\xi_{\Omega,i}\in H(\mathrm{div}) \\ (\xi_{\Omega,N}\cdot n = 0)}} -\frac{1}{2}\int_{\mathcal{D}} \Big(k_\Omega^{-1}|\xi_{\Omega,i} + k_\Omega M(\theta^h)\nabla u^h_{\Omega,i} - k_\Omega\nabla r^h_{\Omega,i}|^2 + |\nabla\cdot\xi_{\Omega,i} - (\nabla\cdot\theta^h)u^h_{\Omega,i} - r^h_{\Omega,i}|^2\Big)dx. \tag{5.23}$$

In order to compute the dual flux variables, we seek $\xi_{\Omega,N},\ \xi_{\Omega,D} \in H(\mathrm{div})$ such that $\xi_{\Omega,N}\cdot n = 0$ on $\partial\mathcal{D}$ satisfying $\forall\delta\xi_N,\ \delta\xi_D \in H(\mathrm{div})$ such that $\delta\xi_N\cdot n = 0$ on $\partial\mathcal{D}$

$$\int_{\mathcal{D}} \Big(k_\Omega^{-1}\xi_{\Omega,i}\cdot\delta\xi_i + (\nabla\cdot\xi_{\Omega,i})(\nabla\cdot\delta\xi_i)\Big)dx = \int_{\mathcal{D}} \Big((\nabla\cdot\theta^h)u^h_{\Omega,i}\nabla\cdot\delta\xi_i - M(\theta^h)\nabla u^h_{\Omega,i}\cdot\delta\xi_i\Big)dx \tag{5.24}$$

and via their Raviart-Thomas Finite Element approximations $\xi^h_{\Omega,i}$'s, we derive the upper bound of the adjoint errors in the energy-norm

$$\|\!|r_{\Omega,i} - r^h_{\Omega,i}|\!\|^2_\Omega \leq \int_{\mathcal{D}} \Big(k_\Omega^{-1} |\xi^h_{\Omega,i} + k_\Omega M(\theta^h) \nabla u^h_{\Omega,i} - k_\Omega \nabla r^h_{\Omega,i}|^2 + |\nabla \cdot \xi^h_{\Omega,i} - (\nabla \cdot \theta^h) u^h_i - r^h_{\Omega,i}|^2 \Big) dx. \tag{5.25}$$

Eventually, by plugging (5.21) and (5.25) into (5.10), we are able to explicitly compute the upper bound $\overline{E}$ of the error in the shape gradient.

6 Numerical results

We present some numerical results of the application of the Certified Descent Algorithm (CDA) to the problem of Electrical Impedance Tomography. We remark that the simulations presented in this paper are based on a mesh moving approach for the deformation of the domain (Algorithm 3 - step 7). Thus, the procedure does not allow for topological changes and the correct number of inclusions within the material has to be fixed at the beginning of the algorithm. In order to account for the nucleation of new inclusions or the merging of existing ones, a mixed approach based on topological and shape gradients may be followed as suggested in [15]. For the rest of this section, we will consider several examples where the shape and the location of the inclusions evolve under the assumption that the number of subregions inside $\mathcal{D}$ is *a priori* fixed and known.

Before running the shape optimization algorithm, we identify a set of consistent boundary conditions (g, U_D) for the state problems (5.5). First, we set a Neumann boundary condition g on $\partial\mathcal{D}$ for the flux; in order to impose the Dirichlet condition on the potential, we iteratively solve the Neumann state problem by subsequently refining the mesh until a very fine error estimate in the energy-norm is achieved. The trace of the resulting solution $u_{\Omega,N}$ on $\partial\mathcal{D}$ is eventually picked as boundary datum U_D for the Dirichlet state problem.
All the numerical results were obtained using `FreeFem++` [14].

6.1 Numerical assessment of the goal-oriented estimator

We consider the configuration in figure 1, where $\mathcal{D} \coloneqq \{(x,y) \mid x^2+y^2 \leq \rho_E^2\}$ and $\Omega \coloneqq \{(x,y) \mid x^2+y^2 \leq \rho_I^2\}$. The values for the physical parameters are $\rho_E = 5$, $\rho_I = 4$, $k_E = 1$ and $k_I = 10$. The boundary datum for the Neumann problem (5.1) reads as $g = \cos(M\vartheta)$, $M = 5$. Using a polar coordinate system (ρ, ϑ), we can compute the following analytical solution:

$$u_{\Omega,N} = \begin{cases} C_0 J_M\left(-i\rho k_I^{-\frac{1}{2}}\right)\cos(M\vartheta) & , \ \rho \in [0, \rho_I] \\ \left[C_1 J_M\left(-i\rho k_E^{-\frac{1}{2}}\right) + C_2 Y_M\left(-i\rho k_E^{-\frac{1}{2}}\right)\right]\cos(M\vartheta) & , \ \rho \in (\rho_I, \rho_E] \end{cases}$$

where $J_M(\cdot)$ and $Y_M(\cdot)$ respectively represent the first- and second-kind Bessel functions of order M. The constants $C_0, \ldots, C_2$ are detailed in table 1.

For the approximation of the state equations (5.5), we consider both $\mathbb{P}^1$ and $\mathbb{P}^2$ Lagrangian Finite Element functions. In figures 2A and 2B, we present a comparison between the analytical error due to the discretization and the corresponding estimates arising from the complementary energy

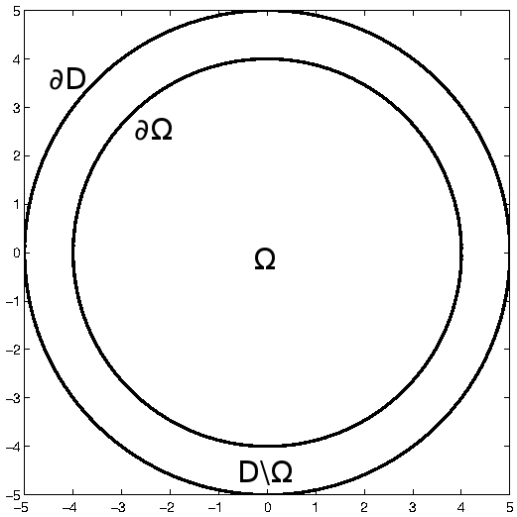

Figure 1: Test case for the Electrical Impedance Tomography. Circular inclusion Ω inside the circular body $\mathcal{D}$.

Constant	$\mathbb{R}\mathrm{e}[C_i]$	$\mathbb{I}\mathrm{m}[C_i]$
C_0	$-6.25887182 \cdot 10^{-9}$	$+40.39491005$
C_1	$+1.30145994$	$+0.325482825$
C_2	$+1.49579729 \cdot 10^{-11}$	-1.301459935

Table 1: Constants for the analytical solution.

principle (Section 5.3.1) under uniform mesh refinements. We remark that using $\mathbb{P}^1$ Finite Elements, the estimated convergence rate is nearly 1, whereas using $\mathbb{P}^2$ basis functions for the Finite Element space leads to a convergence rate slightly lower than 2.

In order to construct the estimator for the error in the shape gradient, first we approximate equation (2.8) using $\mathbb{P}^1 \times \mathbb{P}^1$ Lagrangian Finite Element functions. For the discretization of the adjoint equations (5.11), we use the same Finite Element space as for the state problems, whereas the dual fluxes in equations (5.20) and (5.24) are approximated using Raviart-Thomas Finite Element functions. In particular, we choose the space of RT_0 (respectively RT_1) functions when the state and adjoint equations are solved using $\mathbb{P}^1$ (respectively $\mathbb{P}^2$) Finite Elements.

In figure 3, we present the convergence history of the discretization error in the shape gradient, the error in the Quantity of Interest arising from its linearization and the corresponding complementary energy estimates provided in (5.10) using both $\mathbb{P}^1$ (Fig. 3A) and $\mathbb{P}^2$ (Fig. 3B) Finite Element functions. In both figure 3A and figure 3B, we remark that the error in the linearized Quantity of Interest is very similar to the one in the shape gradient. This confirms that the linearization error introduced in (3.2) is negligible with respect to the discretization error due to the Finite Element approximation and the estimator constructed from the linearized Quantity of Interest provides reliable information on the error in the shape gradient itself.

Figure 3A shows the evolution of the error in the Quantity of Interest with respect to the number of Degrees of Freedom of the problem under uniform mesh refinements. The error estimator shows an

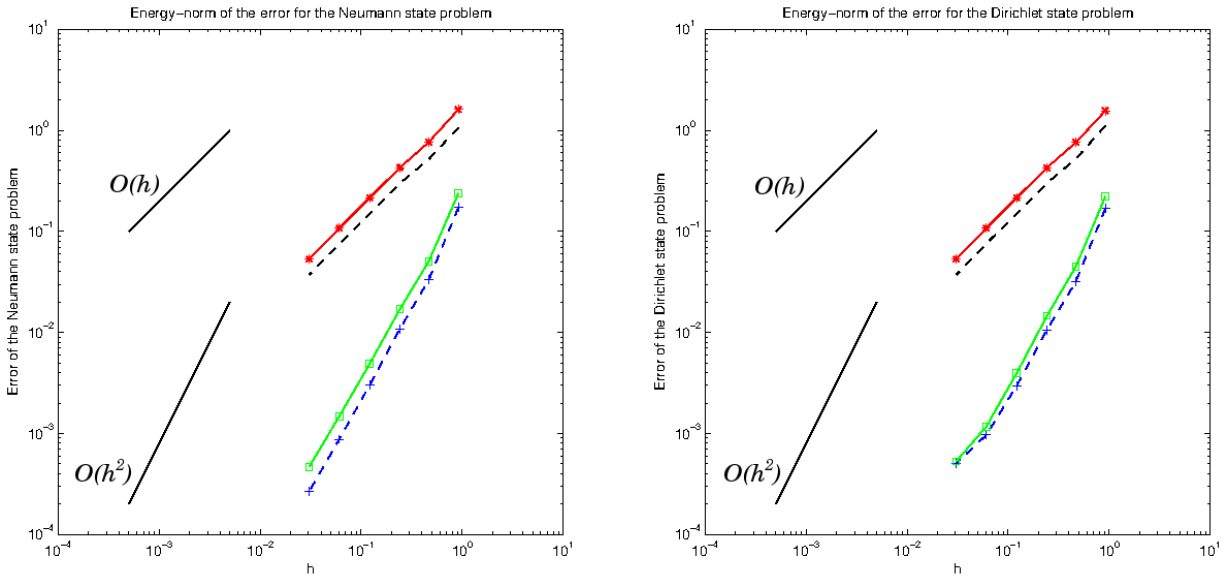

(A) Neumann problem. **(B)** Dirichlet problem.

Figure 2: Comparison of the convergence rates with respect to the mesh size h for the (A) Neumann and (B) Dirichlet state equations. Analytical errors using $\mathbb{P}^1$ (black dash) and $\mathbb{P}^2$ (blue cross) Lagrangian Finite Element functions; error estimates based on the complementary energy principle using $\mathbb{P}^1$ (red star) and $\mathbb{P}^2$ (green square) Lagrangian Finite Element functions.

evolution which is analogous to the one of the analytical error in the shape gradient, thus we verify that an upper bound for the error in the Quantity of Interest is derived. Nevertheless, when dealing with $\mathbb{P}^2$ Lagrangian Finite Element functions (Fig. 3B), the resulting error estimator for the Quantity of Interest underestimates the error in the shape gradient. This phenomenon may be caused by the error due to the approximation of the geometry that has not been accounted for in this work. As a matter of fact, in [20] Morin *et al.* observe that increasing the accuracy of the PDE approximation is useless if the expected geometrical error is higher than the one due to the discretization of the state problem. For this reason, in the following simulations, we stick to low-order Finite Element approximations ($\mathbb{P}^1 - RT_0$) since using higher-order elements would prevent from getting a certified upper bound of the error in the shape gradient which is crucial for the application of the Certified Descent Algorithm.

6.2 1-mesh and 2-mesh reconstruction strategies

We may now apply the CDA to identify the unknown inclusion Ω inside the circular domain $\mathcal{D}$ using one boundary measurement. The initial inclusion is a circle of radius $\rho_{ini} = 2$ and the associated computational mesh counting 472 triangles is displayed in figure 4A.
It is well-known in the literature (see [3]) that using the same computational domain for both solving the state problem and computing a descent direction may lead to poor optimized shapes. In figures 4B and 4C we present the computational domains obtained using respectively a 1-mesh strategy to

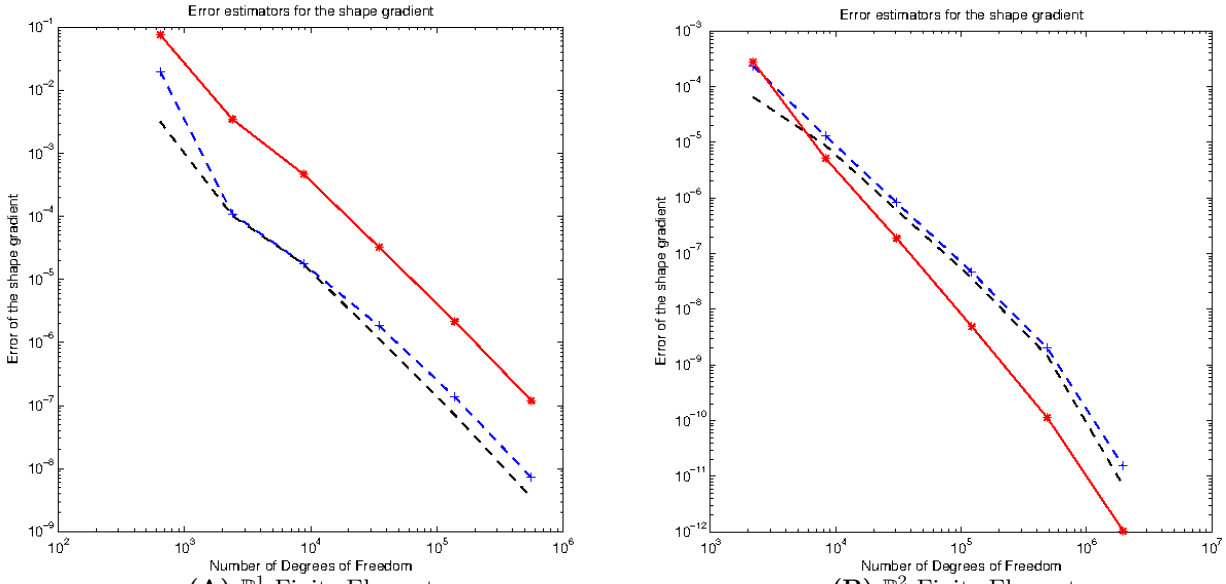

(A) $\mathbb{P}^1$ Finite Element. **(B)** $\mathbb{P}^2$ Finite Element.

Figure 3: Comparison of the convergence rates with respect to the number of Degrees of Freedom for the error in the Quantity of Interest using (A) $\mathbb{P}^1$ and (B) $\mathbb{P}^2$ Lagrangian Finite Element functions. Analytical error in the shape gradient (black dash); error in the linearized Quantity of Interest (blue cross); error estimator for the Quantity of Interest using the complementary energy principle (red star).

compute both the solutions $u^h_{\Omega,i}$'s and the descent direction θ^h and a 2-mesh approach in which the state equations are solved on a fine mesh whereas θ^h is computed on a coarser domain. A comparison of the reconstructed interfaces after 24 and 25 iterations is reported in figure 4D and as expected we observe that the 1-mesh algorithm provides a poor approximation of the inclusion whereas the 2-mesh strategy is able to precisely retrieve the boundary along which the conductivity k_Ω is discontinuous. Figures 4E and 4F confirm what was already observed by zooming on the local behavior of the interfaces and highlighting the oscillatory nature of the 1-mesh reconstruction. In figure 5A, we report the evolution of the objective functional with respect to the number of iterations using the two discussed approaches. It is straightforward to observe that the CDA identifies a genuine descent direction at each iteration, generating a sequence of minimizing shapes such that the objective functional $J(\Omega)$ is monotonically decreasing. Moreover, the error estimate in the shape gradient is also used to construct a guaranteed stopping criterion for the overall optimization strategy which automatically ends when $|\langle d_h J(\Omega), \theta^h \rangle| + \overline{E} < \texttt{tol}$ for an *a priori* fixed tolerance. Even though both versions of the algorithm generate shapes for which the functional is monotonically decreasing, only the 2-mesh strategy is able to precisely identify the target inclusion. For this reason, in the following sections we will focus only on the 2-mesh approach.

Besides the theoretical improvement of the Boundary Variation Algorithm discussed so far, an advantage of the CDA lies in the possibility of using relatively coarse meshes to identify certified descent directions. In figure 5B we observe that the number of Degrees of Freedom remains small until the reconstructed interface approaches the real inclusion, that is coarse meshes prove to be reliable dur-

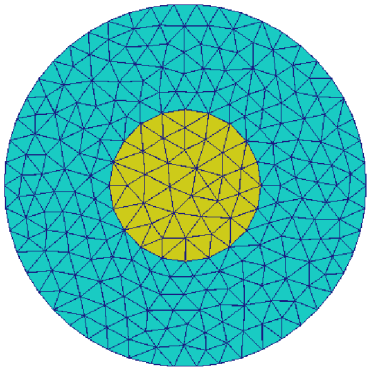

(A) 472 elements.

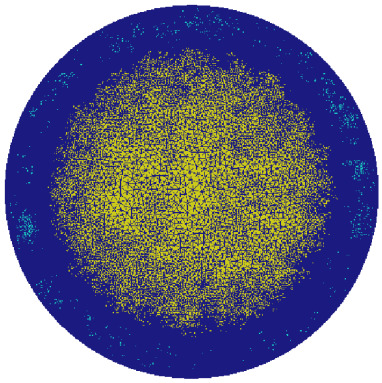

(B) 178047 elements.

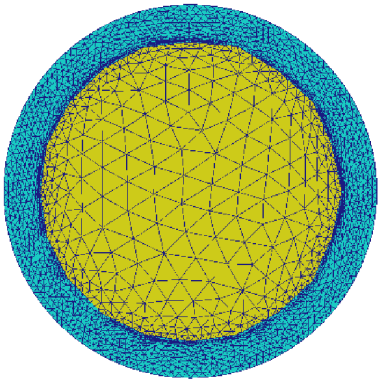

(C) 66833 elements.

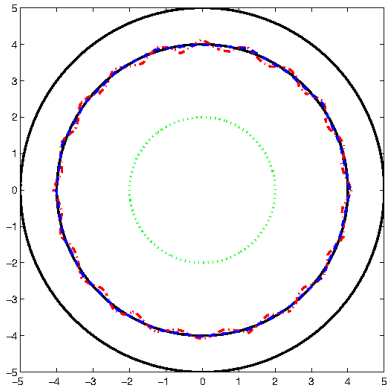

(D) Reconstructed interface.

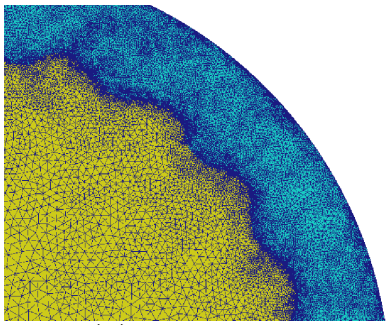

(E) 1-mesh interface.

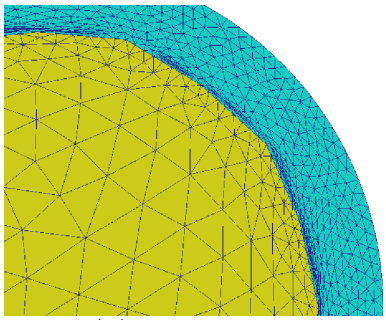

(F) 2-mesh interface.

Figure 4: Comparison of 1-mesh and 2-mesh reconstruction strategies. (A) Initial mesh. (B) Final mesh using 1-mesh strategy. (C) Final mesh using 2-mesh strategy. (D) Initial configuration (dotted green), target inclusion (solid black) and reconstructed interfaces using 1-mesh (dot-dashed red) and 2-mesh (dashed blue) strategies. (E) Zoom of the reconstructed interface using 1-mesh strategy. (F) Zoom of the reconstructed interface using 2-mesh strategy.

ing the initial iterations of the algorithm. Thus, another important feature of the Certified Descent Algorithm is the ability of certifying the reliability of coarse meshes for the identification of genuine descent directions for a shape functional, reducing the overall computational effort of the algorithm coupled with the *a posteriori* estimators during the initial phase of computation.

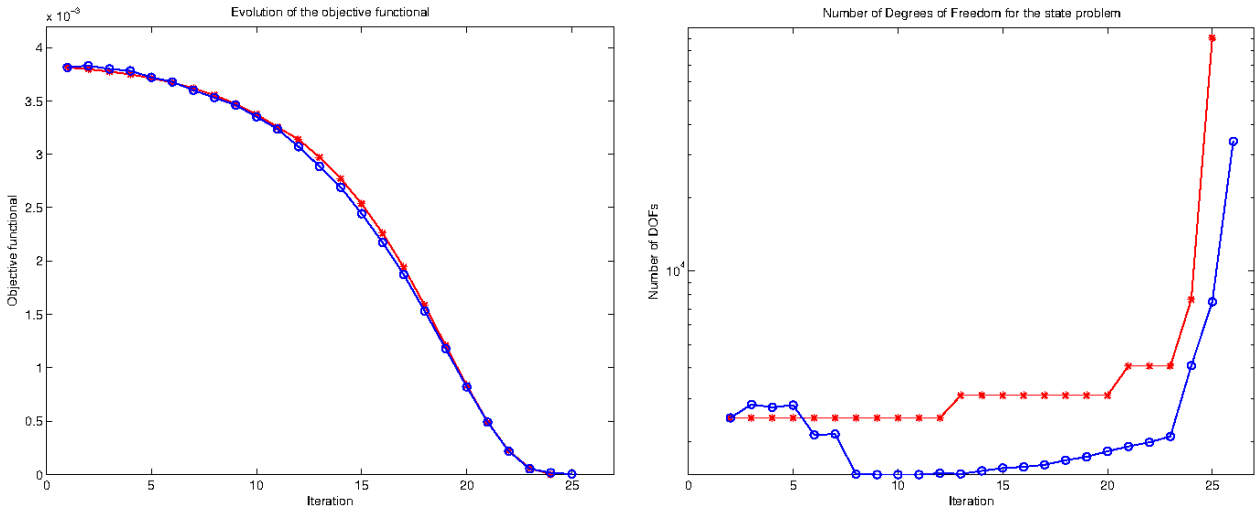

(A) Objective functional. **(B)** Number of Degrees of Freedom.

Figure 5: Comparison of 1-mesh (red star) and 2-mesh (blue circle) reconstruction strategies. (A) Evolution of the objective functional. (B) Number of Degrees of Freedom.

6.3 A more involved test case

In the previous section, we applied the Certified Descent Algorithm on a simple

test case and we were able to retrieve a precise description of the interface $\partial\Omega$. This was mainly due to the fact that the inclusion Ω was located near the external boundary $\partial\mathcal{D}$ where the measurements are performed. In this section, we consider a more involved test case: on the one hand, we break the symmetry of the problem by considering the initial and target configurations in figure 6A; on the other hand, we highlight the difficulties of precisely identifying the boundary of an inclusion when its position is far away from $\partial\mathcal{D}$.

As observed in the previous section, the evolution of the objective functional is monotonically decreasing (Fig. 6B), meaning a genuine descent direction is identified at each iteration of the optimization procedure. The final value of the approximated objective functional is $\mathcal{O}(10^{-5})$, in agreement with the zero value in the analytical optimal configuration of the inclusion.
Moreover, the evolution of the number of Degrees of Freedom (Fig. 6C) shows that coarse meshes prove to be reliable during initial iterations. The size of the problem remains small for several successive iterations and only when approaching the configuration for which the criterion $|\langle d_h J(\Omega), \theta^h\rangle| + \overline{E}$ fulfills a given tolerance $\texttt{tol} = 10^{-6}$ the CDA performs multiple mesh refinements increasing the number of Degrees of Freedom.

In figure 6A, we observe that the part of the interface closest to $\partial\mathcal{D}$ is well identified using the Certified Descent Algorithm with one boundary measurement. Nevertheless when moving away from the external boundary, the precision of the reconstructed interface decreases and the algorithm is not able to precisely identify the whole inclusion. The uncertainty of the reconstruction in the central region of $\mathcal{D}$ is mainly due to the ill-posedness of the inverse problem. As a matter of fact, state problems (5.1) and (5.2) are elliptic equations thus the effect of the boundary conditions becomes less and less important moving away from $\partial\mathcal{D}$. In next section, we present a strategy to improve the

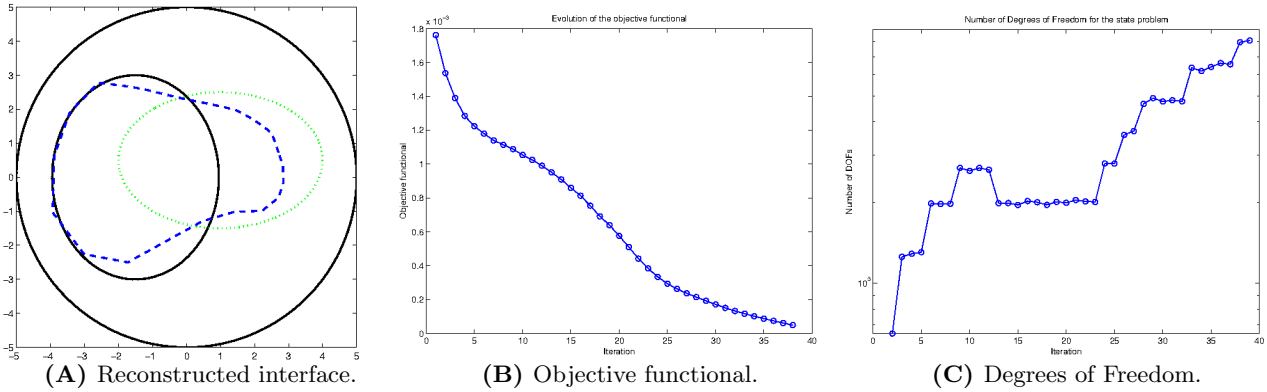

(A) Reconstructed interface. **(B)** Objective functional. **(C)** Degrees of Freedom.

Figure 6: Certified Descent Algorithm using one measurement. (A) Initial configuration (dotted green), target inclusion (solid black) and reconstructed interface (dashed blue). (B) Evolution of the objective functional. (C) Number of Degrees of Freedom.

CDA by using several boundary measurements to retrieve a better approximation of the inclusion. In particular, we will highlight how this additional information allows to exactly reconstruct the interface almost everywhere, except for a small region near the middle of the domain $\mathcal{D}$. A possible workaround to this issue and to the low resolution of the reconstruction in the center of the computational domain is proposed by Ammari *et al.* in [4], where a hybrid imaging method arising from the coupling of electromagnetic tomography with acoustic waves is described.

6.4 The case of multiple boundary measurements

In [29], the authors prove that from an analytical point of view, one measurement is sufficient to uniquely reconstruct the inclusion within the Calderón's problem. Other analytical results on this topic are presented in [1]. Nevertheless, from a numerical point of view, it is known that multiple measurements are required to have a good approximation of the Electrical Impedance Tomography identification problem. In this section, we present several tests of the previously described algorithm using multiple boundary measurements. In particular, we consider $D = 10$ measurements such that $\forall j = 0, \dots, D-1$

$$g_j(x,y) = (x + a_j y)^{b_j} a_j^{c_j} \quad , \quad a_j = 1 + 0.1j \quad , \quad b_j = \frac{j+1}{2} \quad , \quad c_j = j - 2\left\lfloor \frac{j}{2} \right\rfloor$$

and we use them to test the following cases:

(i) one inclusion in a circular domain (Fig. 7A-7C);

(ii) one inclusion in a square domain (Fig. 7D-7F);

(iii) two inclusions in a circular domain (Fig. 7G-7I);

(iv) two inclusions in a square domain (Fig. 8A-8C).

First, we consider the test case introduced in the previous section, where the domain is the circle $\mathcal{D} := \{(x, y) \mid x^2 + y^2 \leq 25\}$ and the inclusion is the solid black line in figure 6A. Then, we present a simulation in which the body is the square $\mathcal{D} := [-4, 4]^2$ featuring a single polygonal inclusion (Fig. 7F). Eventually, we propose two cases with multiple inclusions (Fig. 7I and 8C): in both simulations, we assume that the number of inclusions is known *a priori* and equals 2 and that the conductivity k_Ω has only two values, one inside the inclusions and one for the background. As expected, the use of multiple measurements provides additional information to better reconstruct the target interfaces (Fig. 7C, 7F, 7I and 8C). We observe that the CDA is able to reconstruct the inclusions near the boundary $\partial\mathcal{D}$ of the domain whereas the inner interfaces appear more difficult to identify and with a less precise outcome. This phenomenon is due to the severe ill-posedness of the problem and the diffusive nature of the state equation is responsible for the loss of the information in the center of $\mathcal{D}$, even when using several measurements. In particular, we remark that the final interface in figure 7F still presents two kinks from the initial configuration: this is mainly due to the aforementioned phenomenon and may be bypassed by choosing a regularizing scalar product. However, this approach would lead to a global smoothing of the reconstructed interface, including a loss of information about the potential sharp physical corners of the polygonal inclusion.

As previously remarked, figure 9A confirms the monotonically decreasing behavior of the objective functional with respect to the iterations of the algorithm. Moreover, the quantitative information associated with the estimator of the error in the shape gradient allows to derive a reliable stopping criterion for the optimization procedure which results to be fully-automatic.
Eventually, coarse meshes are proved to be reliable for the computation during the initial iterations when the guessed position and shape of the inclusion is very unlikely to be precise. Within this context, even few Degrees of Freedom provide enough information to identify a genuine descent direction for the objective functional which we later certify using the discussed goal-oriented procedure. Thus, the same meshes may be used for several iterations increasing the number of Degrees of Freedom only when the descent direction is no more validated (Fig. 9B).

7 Conclusion

In this work, we coupled classical shape optimization techniques with a goal-oriented error estimator for the shape gradient. A guaranteed bound for the error in the shape gradient has been derived by means of a certified *a posteriori* estimator.
On the one hand, introducing an *a posteriori* estimator for the error in the shape gradient provides quantitative information to define a reliable stopping criterion for the overall optimization procedure. Coupling this approach with the 2-mesh shape optimization strategy introduced in [3] results in the novel Certified Descent Algorithm. The CDA is a fully-automatic procedure for certified shape optimization: a validation of the method is presented by means of several test cases for the well-known

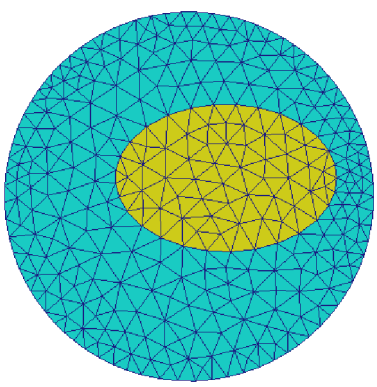

(A) 387 elements.

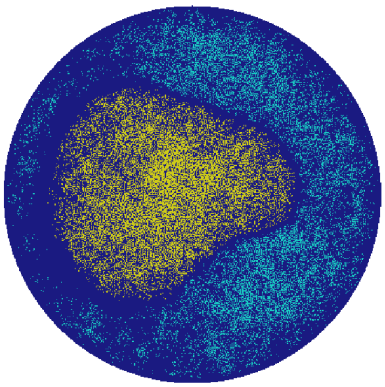

(B) 267578 elements.

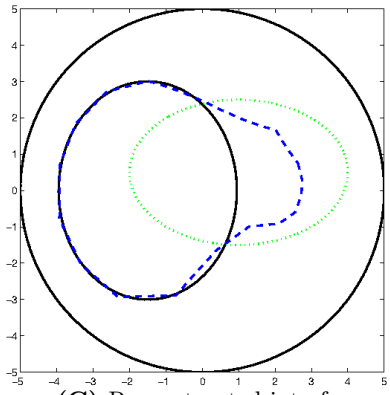

(C) Reconstructed interface.

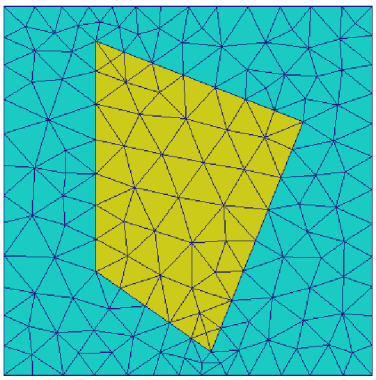

(D) 194 elements.

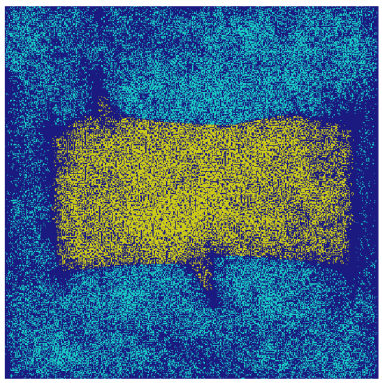

(E) 132040 elements.

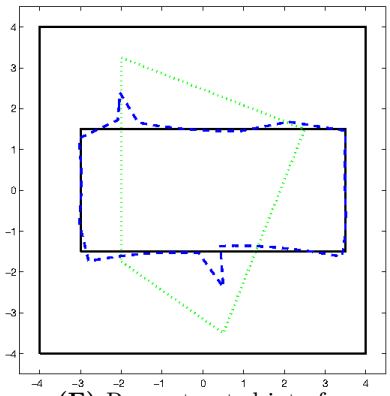

(F) Reconstructed interface.

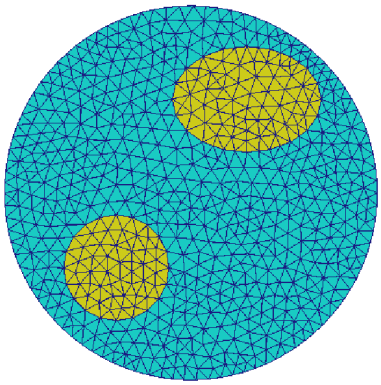

(G) 939 elements.

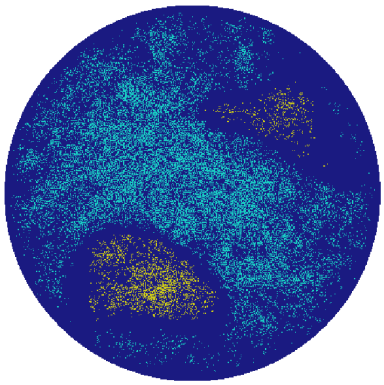

(H) 428251 elements.

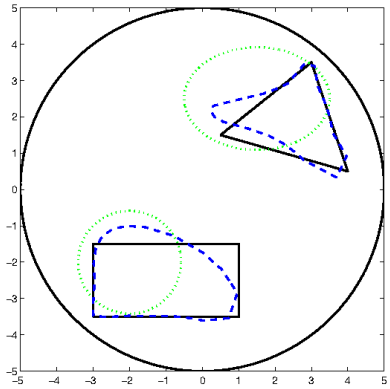

(I) Reconstructed interface.

Figure 7: Certified Descent Algorithm using multiple measurements: test cases (i)-(iii). Left: Initial mesh. Center: Final mesh. Right: Initial configuration (dotted green), target inclusion (solid black) and reconstructed interface (dashed blue).

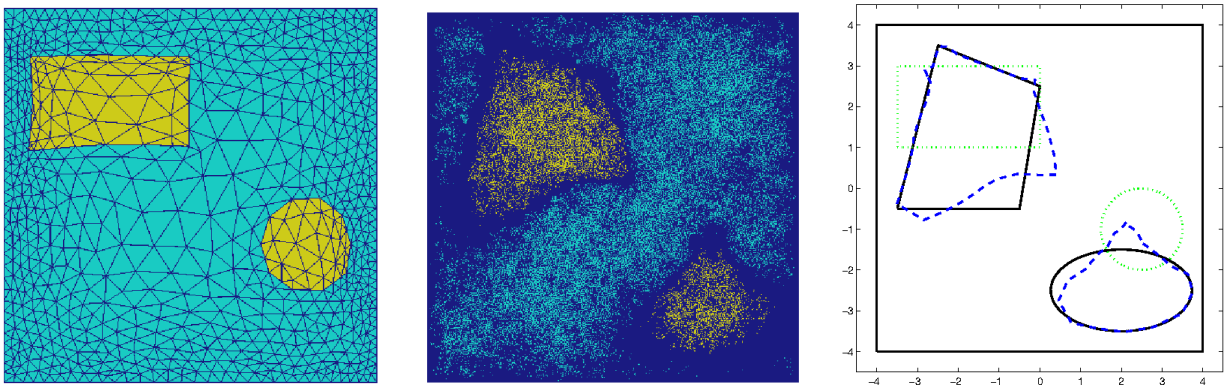

(A) 1616 elements. **(B)** 475744 elements. **(C)** Reconstructed interface.

Figure 8: Certified Descent Algorithm using multiple measurements: test case (iv). Left: Initial mesh. Center: Final mesh. Right: Initial configuration (dotted green), target inclusion (solid black) and reconstructed interface (dashed blue).

inverse identification problem of Electrical Impedance Tomography. Another important feature of this method is the ability of identifying a certified descent direction at each iteration thus leading to a monotonically decreasing evolution of the objective functional.

Even though the CDA is able to make coarse meshes reliable to identify a genuine descent direction for the objective functional during the initial iterations, the overall computational cost tends to remain high. As a matter of fact, the major drawback of the described procedure is the necessity of solving the dual flux problems to derive a fully-computable upper bound of the error in the shape gradient. Hence, the Certified Descent Algorithm may result in higher computing times than the Boundary Variation Algorithm applied on fine meshes.

Ongoing research focuses on improving the *a posteriori* estimates for the discretization error in the shape gradient. Promising results are expected by the development of error estimators that only involve the computation of local quantities. Within this framework, accounting for anisotropic mesh adaptivity [23] may lead to discretizations with a lower number of Degrees of Freedom and a better approximation of the physical problem.
Future investigations will focus on the application of the Certified Descent Algorithm to other challenging problems, such as the shape optimization of elastic structures.

References

[1] L. Afraites, M. Dambrine, and D. Kateb. Shape methods for the transmission problem with a single measurement. *Numer. Func. Anal. Opt.*, 28(5-6):519–551, 2007.

[2] F. Alauzet, B. Mohammadi, and O. Pironneau. Mesh adaptivity and optimal shape design for aerospace. In G. Buttazzo and A. Frediani, editors, *Variational Analysis and Aerospace Engineering: Mathematical Challenges for Aerospace Design*, Springer Optimization and Its Applications, pages 323–337. Springer US, 2012.

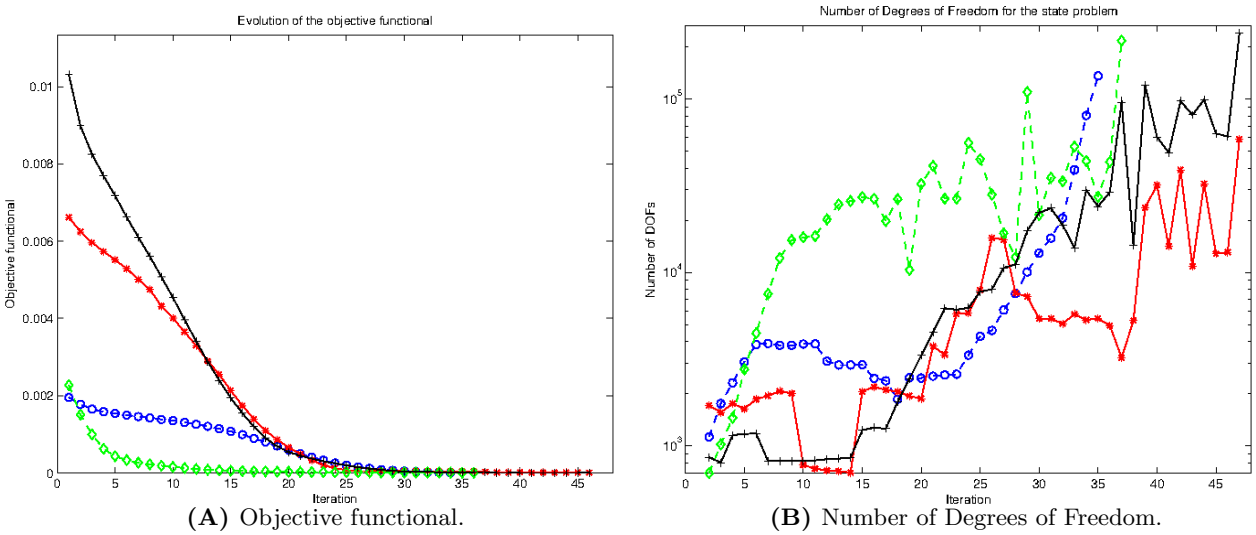

(A) Objective functional. **(B)** Number of Degrees of Freedom.

Figure 9: Certified Descent Algorithm using multiple measurements: test case (i) blue circles; (ii) red stars; (iii) green diamonds; (iv) black crosses. (A) Evolution of the objective functional. (B) Number of Degrees of Freedom.

[3] G. Allaire and O. Pantz. Structural optimization with `FreeFem++`. *Struct. Multidisc. Optim.*, 32(3):173–181, 2006.

[4] H. Ammari, E. Bossy, J. Garnier, and L. Seppecher. Acousto-electromagnetic tomography. *SIAM J. Appl. Math.*, 72(5):1592–1617, 2012.

[5] H. Azegami, S. Kaizu, M. Shimoda, and E. Katamine. Irregularity of shape optimization problems and an improvement technique. In S. Hernandez and C. Brebbia, editors, *Computer Aided Optimization Design of Structures V*, pages 309–326. Computational Mechanics Publications, 1997.

[6] N. Banichuk, F.-J. Barthold, A. Falk, and E. Stein. Mesh refinement for shape optimization. *Struct. Optim.*, 9:46–51, 1995.

[7] L. Borcea. Electrical impedance tomography. *Inverse Prob.*, 18(6):R99, 2002.

[8] A. Calderón. On an inverse boundary value problem. In *Seminar on Numerical Analysis and its Applications to Continuum Physics (Rio de Janeiro 1980)*, pages 65–73. Soc. Brasil. Mat., 1980.

[9] J. Céa. Conception optimale ou identification de formes, calcul rapide de la dérivée directionnelle de la fonction coût. *ESAIM: Mathematical Modelling and Numerical Analysis*, 20(3):371–402, 1986.

[10] M. Cheney, D. Isaacson, and J. Newell. Electrical impedance tomography. *SIAM Rev.*, 41:85–101, 1999.

[11] M. Delfour and J.-P. Zolésio. *Shapes and geometries: analysis, differential calculus, and optimization*. SIAM, Philadelphia, USA, 2001.

[12] G. Dogăn, P. Morin, R. Nochetto, and M. Verani. Discrete gradient flows for shape optimization and applications. *Comput. Methods Appl. Mech. Engrg.*, 196(3740):3898 – 3914, 2007. Special Issue Honoring the 80th Birthday of Professor Ivo Babuka.

[13] T. Grätsch and K.-J. Bathe. Goal-oriented error estimation in the analysis of fluid flows with structural interactions. *Comput. Methods Appl. Mech. Engrg.*, 195:5673–5684, 2006.

[14] F. Hecht. New development in `FreeFem++`. *J. Numer. Math.*, 20(3-4):251–265, 2012.

[15] M. Hintermüller and A. Laurain. Electrical impedance tomography: from topology to shape. *Control Cybern.*, 37(4):913–933, 2008.

[16] R. Hiptmair, A. Paganini, and S. Sargheini. Comparison of approximate shape gradients. *BIT Numerical Mathematics*, pages 1–27, 2014.

[17] N. Kikuchi, K. Chung, T. Torigaki, and J. Taylor. Adaptive Finite Element Methods for shape optimization of linearly elastic structures. *Comput. Method Appl. Mech. Eng.*, 57:67–89, 1986.

[18] R. Kohn and M. Vogelius. Relaxation of a variational method for impedance computed tomography. *Comm. Pure Appl. Math.*, 40(6):745–777, 1987.

[19] A. Laurain and K. Sturm. Domain expression of the shape derivative and application to electrical impedance tomography. Research Report 1863, WIAS, 2013.

[20] P. Morin, R. Nochetto, M. Pauletti, and M. Verani. Adaptive finite element method for shape optimization. *ESAIM: Control Optim. Calc. Var.*, 18:1122–1149, 2012.

[21] J. Oden and S. Prudhomme. Goal-oriented error estimation and adaptivity for the Finite Element Method. *Comput. Math. Appl.*, 41(5-6):735 – 756, 2001.

[22] O. Pantz. Sensibilité de l'équation de la chaleur aux sauts de conductivité. *C. R. Acad. Sci. Paris*, Ser. I(341):333–337, 2005.

[23] G. Porta, S. Perotto, and F. Ballio. Anisotropic mesh adaptation driven by a recovery-based error estimator for shallow water flow modeling. *Int. J. Numer. Meth. Fl.*, 70(3):269–299, 2012.

[24] S. Repin. A posteriori error estimation for variational problems with uniformly convex functionals. *Math. Comput.*, 69(230):481–500, 2000.

[25] J. Roche. Adaptive Newton-like method for shape optimization. *Control Cybern.*, 34(1):363–377, 2005.

[26] M. Rüter, T. Gerasimov, and E. Stein. Goal-oriented explicit residual-type error estimates in XFEM. *Comput. Mech.*, 52(2):361–376, 2013.

[27] A. Schleupen, K. Maute, and E. Ramm. Adaptive FE-procedures in shape optimization. *Struct. Multidisc. Optim.*, 19:282–302, 2000.

[28] J. Sokołowski and J. Zolésio. *Introduction to shape optimization: shape sensitivity analysis.* Springer-Verlag, 1992.

[29] J. Sylvester and G. Uhlmann. A global uniqueness theorem for an inverse boundary value problem. *Ann. Math.*, 125:153–169, 1987.

[30] T. Vejchodský. Complementary error bounds for elliptic systems and applications. *Appl. Math. Comput.*, 219(13):7194 – 7205, 2013.

[31] A. Wexler, B. Fry, and M. R. Neuman. Impedance-computed tomography algorithm and system. *Appl. Opt.*, 24(23):3985–3992, 1985.